The onset of zonal modes in two-dimensional Rayleigh–Bénard convection

Philip Winchester[1]†, and Peter D. Howell[1]‡, Vassilios Dallas [1]¶

[1]Mathematical Institute, University of Oxford, Oxford, OX2 6GG, UK

(Received xx; revised xx; accepted xx)

We study the stability of steady convection rolls in 2D Rayleigh–Bénard convection with free-slip boundaries and horizontal periodicity over twelve orders of magnitude in the Prandtl number ($10^{-6} \leqslant Pr \leqslant 10^{6}$) and six orders of magnitude in the Rayleigh number ($8\pi^4 < Ra \leqslant 10^{8}$). The analysis is facilitated by partitioning our modal expansion into so-called even and odd modes. With aspect ratio $\Gamma = 2$, we observe that zonal modes (with horizontal wavenumber equal to zero) can emerge only once the steady convection roll state consisting of even modes only becomes unstable to odd perturbations. We determine the stability boundary in the (Pr, Ra)-plane and observe remarkably intricate features corresponding to qualitative changes in the solution, as well as three regions where the steady convection rolls lose and subsequently regain stability as the Rayleigh number is increased. We study the asymptotic limit $Pr \to 0$ and find that the steady convection rolls become unstable almost instantaneously, eventually leading to non-linear relaxation osculations and bursts, which we can explain with a weakly non-linear analysis. In the complementary large-Pr limit, we observe that the zonal modes at the instability switch off abruptly at a large, but finite, Prandtl number.

Key words: Bénard convection, bifurcations, low-dimensional models

1. Introduction

Rayleigh–Bénard convection typically begins with a steady cellular pattern (for example, rolls, squares or hexagons), and the stability of these cellular patterns has been studied for decades (Busse 1967, 1983; Busse & Bolton 1984; Bolton & Busse 1985; Rucklidge & Matthews 1996; Paul *et al.* 2012). In a 2D periodic box, the cellular pattern takes the form of convection rolls which are invariant under reflections both in the vertical plane that separates them and in the horizontal mid-plane. The vertical mirror symmetry can be broken in a pitchfork bifurcation, generating a net zonal flow in which any motion in one direction at the top will be balanced by an equal and opposite motion at the bottom (Rucklidge & Matthews 1996). The physical mechanism behind this instability is well understood (Thompson 1970; Busse 1983; Howard & Krishnamurti 1986). Suppose a pair of initially symmetric rolls tilts over, say to the right. The rising plume will now transport rightward momentum to the top of the layer, while the descending plume will transport leftward momentum to the bottom of the layer. The resulting horizontal streaming motion causes a net zonal flow across the layer, which may be enough to

† Email address for correspondence: winchester@maths.ox.ac.uk
‡ Email address for correspondence: howell@maths.ox.ac.uk
¶ Email address for correspondence: dallas@maths.ox.ac.uk

sustain the original tilt of the rolls. The vertical mirror symmetry may also be broken in a Hopf bifurcation, leading to oscillations in which the direction of the zonal flow alternates (Landsberg & Knobloch 1991; Proctor & Weiss 1993; Rucklidge & Matthews 1996).

Large scale zonal flow in buoyancy-driven convection has been found in the atmosphere of Jupiter (Heimpel *et al.* 2005; Kong *et al.* 2018; Kaspi *et al.* 2018), the Earth's oceans (Maximenko *et al.* 2005; Richards *et al.* 2006; Nadiga 2006), nuclear fusion devices (Diamond *et al.* 2005; Fujisawa 2008), and laboratory experiments (Zhang *et al.* 2020; Read *et al.* 2015; Krishnamurti & Howard 1981). The shearing instability which generates this net zonal flow has been studied both in the full Boussinesq equations (Rucklidge & Matthews 1996; Paul *et al.* 2012) and in several modal truncations (Howard & Krishnamurti 1986; Hermiz *et al.* 1995; Horton *et al.* 1996; Rucklidge & Matthews 1996; Aoyagi *et al.* 1997; Berning & Spatschek 2000). More recently, prominent zonal flow has been found to greatly suppress convective heat transfer (Goluskin *et al.* 2014) and depend strongly on the geometry of the studied domain (Wang *et al.* 2020; Fuentes & Cumming 2021).

Winchester *et al.* (2021) showed how zonal flow can emerge at Prandtl number $Pr = 30$ in two-dimensional Rayleigh–Bénard convection through a sequence of bifurcations as Rayleigh number Ra increases. First the system undergoes a Hopf bifurcation, resulting in an oscillating zonal flow, which then grows in amplitude until the system becomes attracted to one of the two symmetric metastable shearing states. At intermediate Rayleigh numbers, the system performs apparently random-in-time transitions between these states, resulting in abrupt zonal flow reversals. As Ra increases further, the system ultimately converges to one of the shearing states, resulting in a persistent zonal flow.

In this article, we study in further detail the initial emergence of zonal modes, with horizontal wavenumber equal to zero. We analyse the stability of steady two-dimensional convective rolls over twelve orders of magnitude in the Prandtl number ($10^{-6} \leqslant Pr \leqslant 10^{6}$) and six orders of magnitude in the Rayleigh number ($8\pi^4 < Ra \leqslant 10^{8}$). We focus on the case of free-slip boundary conditions on the horizontal boundaries and periodic boundary conditions on the vertical boundaries in a rectangular domain of width-to-height aspect ratio $\Gamma = 2$.

The equations governing Rayleigh–Bénard convection and our modal decomposition are outlined in §2. In §3, we describe the numerical scheme used to calculate steady states and their stability. We determine the stability boundary in the (Pr, Ra)-plane and demonstrate how remarkably intricate features on the boundary correspond to qualitative changes in the solution. In §4 the regime of small Prandtl number is examined in more detail, by using formal asymptotic analysis to construct a system of two amplitude equations in the limit $Pr \to 0$. The complementary limit of $Pr \to \infty$ is studied in §5. Concluding remarks on the article's findings appear in §6.

2. Problem formulation

We consider two-dimensional Rayleigh–Bénard convection governed by the dimensionless equations

$$\nabla^2\psi_t + \{\psi, \nabla^2\psi\} = RaPr\theta_x + Pr\nabla^4\psi, \tag{2.1a}$$

$$\theta_t + \{\psi, \theta\} = \psi_x + \nabla^2\theta, \tag{2.1b}$$

where $\psi(x, y, t)$ is the streamfunction and $\theta(x, y, t)$ is the field of temperature fluctuations from the heat-conducting temperature profile $T = 1 - y + \theta$. Here, subscripts denote

partial derivatives, and $\{f,g\} = f_x g_y - g_x f_y$ is the usual Poisson bracket. Equations (2.1) have been non-dimensionalised using d, d^2/κ and ΔT as the relevant scales for length, time and temperature, respectively, where d is the height of the fluid layer, κ is the thermal diffusivity and ΔT is the temperature difference imposed across the layer. The two dimensionless parameters in the system (2.1) are the Prandtl and Rayleigh numbers

$$Pr = \frac{\nu}{\kappa}, \qquad Ra = \frac{\alpha \Delta T g d^3}{\nu \kappa}, \tag{2.2}$$

where ν is the kinematic viscosity, α is the thermal expansion coefficient, and g is the gravitational acceleration.

The dimensionless spatial domain of our problem is $(x,y) \in [0,\Gamma]\times[0,1]$, where Γ is the width-to-height aspect ratio. The aspect ratio in this study is fixed at $\Gamma = 2$. At the lower ($y = 0$) and upper ($y = 1$) boundaries the temperature satisfies isothermal conditions while the velocity field satisfies no-penetration and stress-free boundary conditions, i.e.

$$\theta\big|_{y=0,1} = 0, \qquad \psi\big|_{y=0,1} = \psi_{yy}\big|_{y=0,1} = 0, \tag{2.3}$$

and periodic boundary conditions are imposed in the x-direction.

Given the above boundary conditions, it is convenient to decompose the streamfunction into basis functions with Fourier modes in the x-direction and sine modes in the y-direction, viz.

$$\begin{aligned}\psi(x,y,t) &= \sum_{k_x\in\mathbb{Z}} \sum_{k_y\in\mathbb{Z}_{>0}} \widehat{\psi}_{k_x,k_y}(t) \mathrm{e}^{2\pi \mathrm{i} k_x x/\Gamma} \sin(\pi k_y y) \\ &= \sum_{k_x,k_y} \widehat{\psi}_{k_x,k_y}(t)\phi_{k_x,k_y}(x,y),\end{aligned} \tag{2.4}$$

where $\widehat{\psi}_{k_x,k_y}$ is the amplitude of the (k_x,k_y) mode of ψ, and we have the constraint $\widehat{\psi}_{k_x,k_y} = \widehat{\psi}^*_{-k_x,k_y}$ (with the star denoting complex conjugation). We decompose θ in the same way.

Rayleigh (1916) has shown that the static conduction state ($\psi = \theta = 0$) bifurcates supercritically to a steady pattern of counter-rotating convection rolls vertically spanning the layer ($k_y = 1$) when $Ra > Ra_c$ with

$$Ra_c = \min_{k_x}\left(\frac{\pi^4}{4\Gamma^4}\frac{(4k_x^2+\Gamma^2)^3}{k_x^2}\right). \tag{2.5}$$

The minimum is taken over integer wavenumbers k_x, and occurs at $k_x = 1$ provided that $\Gamma < 2^{4/3}\sqrt{1+2^{2/3}} \approx 4.05$. Consequently, for our set-up with $\Gamma = 2$, the modes $\widehat{\psi}_{1,1}$ and $\widehat{\theta}_{1,1}$ from Eq. (2.4) become excited through a supercritical pitchfork bifurcation at $Ra_c = 8\pi^4$. In the remainder of the article, we refer to the resulting steady pattern as the *steady convection roll state* (SCRS). An instance of the SCRS with the parameters $(Pr, Ra) = (1, 10^5)$ is shown in Figure 1.

A further decomposition which will aid our analysis is to partition the modes into *odd modes* indicated by the letter O with $k_x + k_y \in 2\mathbb{Z}+1$, and *even modes* indicated by the letter E with $k_x + k_y \in 2\mathbb{Z}$ similarly to previous studies (Chandra & Verma 2011; Verma *et al.* 2015). Consistently with this notion of odd and even modes, we decompose

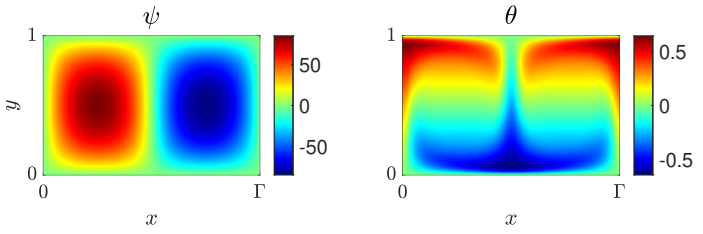

Figure 1: The SCRS calculated with the parameters $(Pr, Ra) = (1, 10^5)$ using the numerical scheme outlined in Appendix A.

ψ as

$$\psi^O(x,y,t) = \frac{1}{2}[\psi(x,y,t) + \psi(x+\Gamma/2, 1-y, t)], \tag{2.6a}$$

$$\psi^E(x,y,t) = \frac{1}{2}[\psi(x,y,t) - \psi(x+\Gamma/2, 1-y, t)], \tag{2.6b}$$

and similarly for θ^O and θ^E. Thus, ψ^O and θ^O consist only of odd modes as defined above, while ψ^E and θ^E consist only of even modes. Applying the decomposition (2.6) to equations (2.1), we find that

$$\nabla^2\psi^O_t + \{\psi^E, \nabla^2\psi^O\} + \{\psi^O, \nabla^2\psi^E\} = RaPr\theta^O_x + Pr\nabla^4\psi^O, \tag{2.7a}$$

$$\theta^O_t + \{\psi^E, \theta^O\} + \{\psi^O, \theta^E\} = \psi^O_x + \nabla^2\theta^O, \tag{2.7b}$$

and

$$\nabla^2\psi^E_t + \{\psi^E, \nabla^2\psi^E\} - RaPr\theta^E_x - Pr\nabla^4\psi^E = -\{\psi^O, \nabla^2\psi^O\}, \tag{2.8a}$$

$$\theta^E_t + \{\psi^E, \theta^E\} - \psi^E_x - \nabla^2\theta^E = -\{\psi^O, \theta^O\}. \tag{2.8b}$$

We observe that (ψ^O, θ^O) satisfy the linear PDEs (2.7), with coefficients that depend on (ψ^E, θ^E), while (ψ^E, θ^E) satisfy the autonomous non-linear PDEs (2.8), with forcing terms that depend on (ψ^O, θ^O).

At the onset of steady convection the excited modes $\widehat{\psi}_{1,1}$ and $\widehat{\theta}_{1,1}$ are even modes, and indeed the SCRS has the property that $\psi^O \equiv \theta^O \equiv 0$, which remains true as we increase Ra. In this case, the system of equations (2.7)–(2.8) reduces to

$$\nabla^2\psi^E_t + \{\psi^E, \nabla^2\psi^E\} = RaPr\theta^E_x + Pr\nabla^4\psi^E, \tag{2.9a}$$

$$\theta^E_t + \{\psi^E, \theta^E\} = \psi^E_x + \nabla^2\theta^E, \tag{2.9b}$$

where the even modes are decoupled from the odd modes. The SCRS has a reflection symmetry about the vertical line which separates the counter-rotating convection rolls. Without loss of generality, we choose this vertical line to be at $x = 0$. Thus, the steady state solution (ψ^E, θ^E) of the system (2.9) is invariant under the symmetry

$$\psi^E(x,y) \mapsto -\psi^E(-x,y), \qquad \theta^E(x,y) \mapsto \theta^E(-x,y). \tag{2.10}$$

Since the zonal modes $\widehat{\psi}_{0,k_y}$ are x-independent, equation (2.10) implies that $\widehat{\psi}^E_{0,k_y} \equiv 0$. In other words, the SCRS has no zonal flow, and zonal modes can emerge only once the SCRS has become unstable.

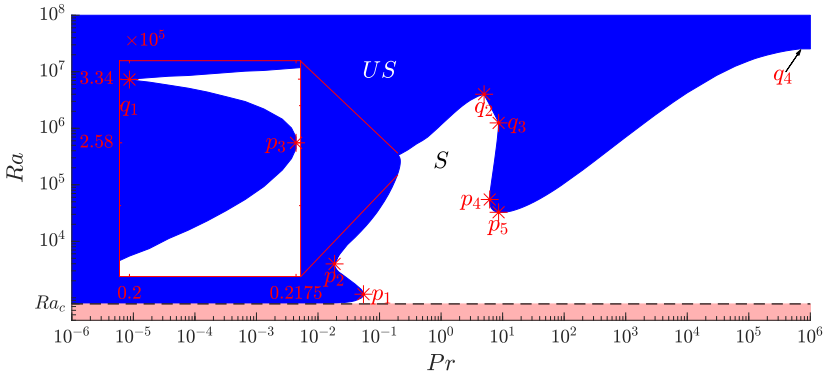

Figure 2: The (Pr, Ra)-plane highlighting when the SCRS is linearly stable (white, S) and unstable (blue, US). Only the static conduction state is stable in the red shaded region below $Ra = Ra_c$ (dashed line). When $Pr \ll 1$, the SCRS becomes unstable at $0 < Ra - Ra_c \ll 1$. The highlighted points in red are at $p_1 = (5.48 \times 10^{-2}, 1.16 \times 10^3)$, $p_2 = (1.81 \times 10^{-2}, 4.12 \times 10^3)$, $p_3 = (0.2175, 2.59 \times 10^5)$, $q_1 = (0.2, 3.32 \times 10^5)$, $q_2 = (4.97, 3.949 \times 10^6)$, $q_3 = (8.58, 1.27 \times 10^6)$, $p_4 = (6.16, 5.43 \times 10^4)$, $p_5 = (9.53, 3.24 \times 10^4)$ and $q_4 = (7 \times 10^5, 2.54 \times 10^7)$. Visualisations of the SCRS at all the points p_i and q_i are given in the Supplementary Material (https://doi.org/10.1017/...).

3. Linear stability analysis

In this section, we present the linear stability analysis of the SCRS. For given values of Pr and Ra, we first solve numerically the steady state problem of Eq. (2.9), following the procedure described in Appendix A. We then exploit the partial decoupling of odd and even modes to consider odd and even perturbations separately. We analyse odd perturbations by setting

$$\begin{aligned}\psi(x,y,t) &= \psi^E(x,y) + \delta \mathrm{e}^{\sigma^o t}\psi^o(x,y)\\ &= \psi^E(x,y) + \delta \mathrm{e}^{\sigma^o t}\sum_{k_x+k_y\in 2\mathbb{Z}+1}\widehat{\psi}^o_{k_x,k_y}\phi_{k_x,k_y}(x,y),\end{aligned} \tag{3.1}$$

$$\begin{aligned}\theta(x,y,t) &= \theta^E(x,y) + \delta \mathrm{e}^{\sigma^o t}\theta^o(x,y)\\ &= \theta^E(x,y) + \delta \mathrm{e}^{\sigma^o t}\sum_{k_x+k_y\in 2\mathbb{Z}+1}\widehat{\theta}^o_{k_x,k_y}\phi_{k_x,k_y}(x,y),\end{aligned} \tag{3.2}$$

where (ψ^E, θ^E) is the SCRS, $\delta \ll 1$ and ψ^o, θ^o consist only of odd modes. By substituting (3.1) into equations (2.1) and linearising with respect to δ, we obtain an eigenvalue problem for the odd growth rates σ^o (see Appendix B for details). Then, we solve this eigenvalue problem numerically and determine that SCRS is unstable with respect to odd perturbations if $\max[\mathcal{R}(\sigma^o)] > 0$. An analogous approach is used to determine the corresponding even growth rates σ^e and thus the stability of the SCRS with respect to even perturbations.

Figure 2 displays the stability of the SCRS in the (Pr, Ra)-plane, highlighting the stable (S) regime in white and the unstable (US) regime in blue. The pink region denotes $Ra < Ra_c$ where the static conduction state is stable. Although the SCRS does become unstable to even perturbations within the region US, we always observe that $\max[\mathcal{R}(\sigma^o)] > \max[\mathcal{R}(\sigma^e)]$ and the dominant unstable perturbation therefore consists of odd modes. Moreover, for $Pr \lesssim 7 \times 10^5$ the most unstable eigenfunction has the property that $\widehat{\psi}^o_{k_x,k_y}$

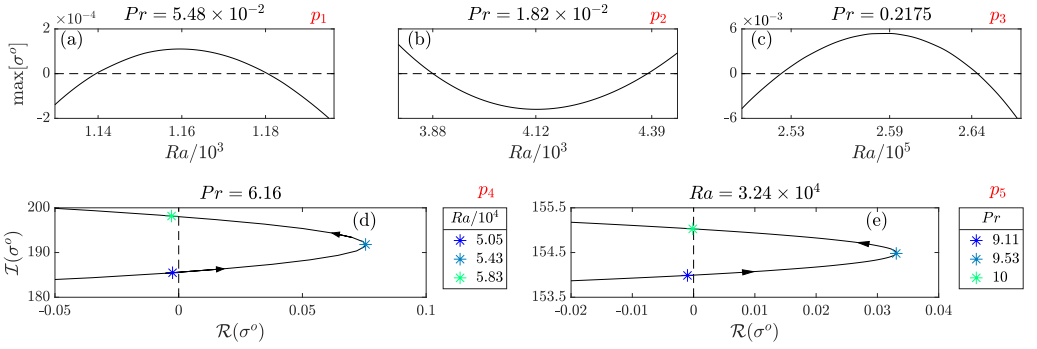

Figure 3: The largest odd growth rate σ^o, plotted with one dimensionless parameter varied and the other fixed. The plots show the behaviour close to each of the points p_i highlighted in figure 2. In (a)–(c) σ^o is real, while in (d) and (e) the motion of σ^o in the complex plane is tracked, with the arrows indicating the direction of increasing Ra or Pr.

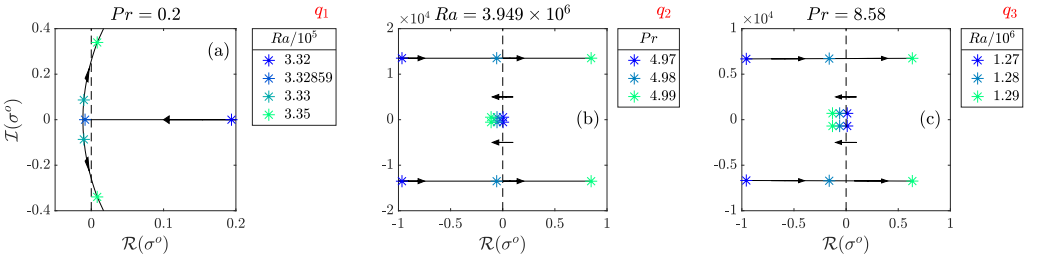

Figure 4: The largest odd growth rate(s) σ^o, plotted with one dimensionless parameter varied and the other fixed. The plots show the behaviour close to each of the points q_i highlighted in figure 2. The motion of σ^o in the complex plane is tracked, with the arrows indicating the direction of increasing Ra or Pr.

and $\mathrm{i}\widehat{\theta}^o_{k_x,k_y}$ are purely real, so that ψ^o and θ^o break the reflection symmetry (2.10). Zonal modes $\widehat{\psi}_{0,k_y}$ with $k_y \in 2\mathbb{Z}+1$ are present in the most unstable perturbation until we reach very large Prandtl numbers (see §5). In particular, we find that the largest scale zonal mode $\widehat{\psi}_{0,1}$ is present in the most unstable eigenfunction at the stability boundary for $Pr \lesssim 7 \times 10^5$, and is the dominant mode for $Pr \lesssim 4.79$ and $8.58 \lesssim Pr \lesssim 40$.

The points p_i annotated in Figure 2 highlight turning points in the stability boundary. The behaviour of σ^o near each such point is plotted in Figure 3. Figure 3(c) shows that, close to $Pr = 0.2$ and with increasing Rayleigh number, a real eigenvalue crosses the origin twice, and the SCRS first loses and then regains stability. The steady state unexpectedly regains stability as the Rayleigh number increases at point p_1 with $Pr \approx 0.055$. Similar behaviour has been observed by Paul *et al.* (2012), with $Pr = 6.8$ and $\Gamma = 2\sqrt{2}$. At point p_2, the opposite occurs with the SRCS first regaining and then losing stability as Ra increases. At points p_4 and p_5 we instead find complex eigenvalues crossing the imaginary axis twice as Ra increases with fixed Pr or *vice versa*.

At each of the points labelled q_i, the stability boundary is not smooth, and there is a qualitative change in the eigenfunction to which the SCRS becomes unstable. Figure 4(a) shows how, with $Pr = 0.2$, the SCRS regains stability with a real eigenvalue crossing zero at $Ra \approx 3.32859 \times 10^5$. With further increase in Ra, the eigenvalue splits into a complex

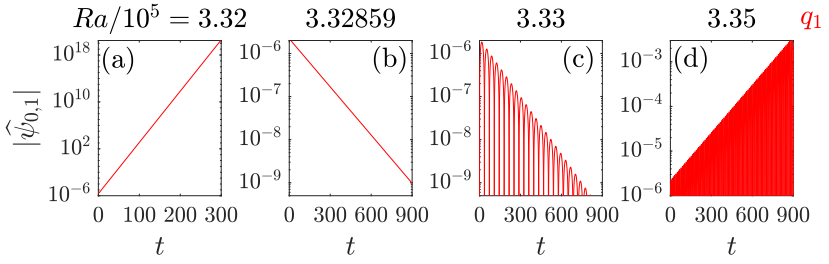

Figure 5: Time series of the $\widehat{\psi}_{0,1}$ mode from the linearised DNS with the right-hand side of (2.8) set to zero. Here we fix $Pr = 0.2$ (q_1) and have $Ra = 3.32 \times 10^5$ (a), $Ra = 3.32859 \times 10^5$ (b), $Ra = 3.33 \times 10^5$ (c) and $Ra = 3.35 \times 10^5$ (d). The initial conditions are the SCRS with a small perturbation.

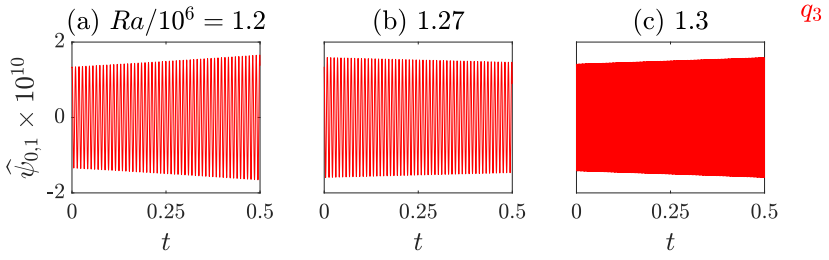

Figure 6: Time series of the $\widehat{\psi}_{0,1}$ mode close to q_3 from the linearised DNS with the right-hand side of (2.8) set to zero. We fix $Pr = 8.57$ and the initial conditions are the SCRS with a small perturbation. Longer time series clearly showing the exponential growth and decay are in the Supplementary Material (https://doi.org/10.1017/...).

conjugate pair, which then recrosses the imaginary axis as the SCRS loses stability in a Hopf bifurcation. The cusp at q_1 occurs when these three events happen simultaneously. These observations have been confirmed with direct numerical simulation (DNS) of the system (2.7)–(2.8), using the pseudospectral scheme described by Winchester *et al.* (2021). Figure 5 shows numerical results for the largest scale odd mode $\widehat{\psi}_{0,1}$ obtained with the right-hand side of (2.8) set to 0, so that we have persistent exponential growth or decay in the odd modes. We observe that, with increasing Ra, the odd perturbations regain stability, then become oscillatory, and finally become unstable again.

Figure 4(c) shows that, with $Pr = 8.58$, the SCRS regains stability through a Hopf bifurcation at $Ra = 1.28 \times 10^6$ but loses stability shortly after at $Ra = 1.29 \times 10^6$ with much larger oscillation frequency. The corner q_3 occurs when these two pairs of eigenvalues cross the imaginary axis simultaneously. Again, this observation has been verified with DNS close to q_3. In Figure 6 we fix $Pr = 8.57$ and see that the odd mode $\widehat{\psi}_{0,1}$ grows at $Ra = 1.2 \times 10^6$, decays at $Ra = 1.27 \times 10^6$, and grows again at $Ra = 1.3 \times 10^6$, but now with a much greater oscillation frequency. As can been seen in Figure 4(b), similar behaviour occurs at corner q_2. The final corner point q_4, which lies in the large-Pr region, will be considered in more detail in §5. Movies showing how the dominant eigenfunction changes at each of the points q_i are included in the Supplementary Material (https://doi.org/10.1017/...).

Figure 2 hints that the Rayleigh number at which the SCRS loses stability approaches

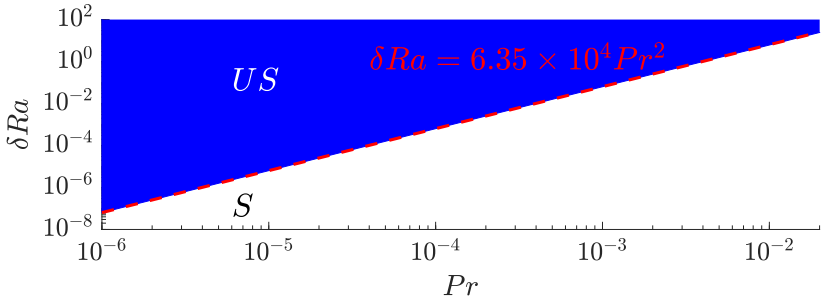

Figure 7: The $(Pr, \delta Ra)$-plane for small Pr highlighting when the SCRS is linearly stable (white, S) and unstable (blue, US). On the vertical axis we plot $\delta Ra = Ra - Ra_c$, where $Ra_c = 8\pi^4$. The red dashed line highlights the power-law $\delta Ra \propto Pr^2$, where the prefactor has been calculated by fitting.

Ra_c as $Pr \to 0$. In Figure 7 we plot

$$\delta Ra := Ra - Ra_c \tag{3.3}$$

versus Pr and indeed see that the stability boundary follows a clear power law with $\delta Ra \propto Pr^2$. When this boundary is crossed, at small Pr the SCRS becomes unstable through a pitchfork bifurcation as a new steady state containing both even and odd modes emerges.

This prediction has been verified with fully nonlinear DNS solving equation (2.1) using the pseudospectral scheme described in Winchester *et al.* (2021). In Figure 8(a) we plot a bifurcation diagram showing the amplitudes of the even mode $\widehat{\psi}_{1,1}$ and the odd mode $\widehat{\psi}_{0,1}$ versus δRa with $Pr = 0.01$. The SCRS emerges at $\delta Ra = 0$ and becomes unstable at $\delta Ra = \delta Ra_c \approx 6.135$ as the new steady state emerges. In Figure 8(b) we plot the time series of $|\widehat{\psi}_{1,1}|$ and $|\widehat{\psi}_{0,1}|$ at $Pr = 0.01$ and $\delta Ra = 10.7$. At this point the mixed steady state has become unstable and the mode $|\widehat{\psi}_{1,1}|$ undergoes non-linear relaxation oscillations whilst $|\widehat{\psi}_{0,1}|$ exhibits bursts that quickly decay away. At $\delta Ra = 2.22 \times 10^3$, the relaxation oscillations and the bursts persist, but are separated by a much slower buildup phase, as shown in Figure 8(c).

In summary, the dynamics at low Prandtl number with $\delta Ra > \delta Ra_c$ can be partitioned into three phases, as follows.

(i) In the first phase we are close to the static conduction state with $|\widehat{\psi}_{1,1}|, |\widehat{\psi}_{0,1}| \approx 0$. However, when $\delta Ra > 0$, the static conduction state is unstable, so that $\widehat{\psi}_{1,1}$ and other even modes grow exponentially.

(ii) The even modes grow until we are in the SCRS. Since $\delta Ra > \delta Ra_c$, the SCRS is unstable to odd perturbations, so that $\widehat{\psi}_{0,1}$ and other odd modes grow exponentially.

(iii) Once $\widehat{\psi}_{1,1}$ and $\widehat{\psi}_{0,1}$ are of comparable amplitude, the system quickly collapses back to the static conduction state and the cycle continues.

These dynamics differ markedly from the chaotic behaviour found close to Ra_c in small-Pr and zero-Pr convection in 3D (Thual 1992; Pal *et al.* 2009). In the following section, we carry out a weakly non-linear analysis to help us explain the observed power-law (see Figure 7) as well as the dynamics of the non-linear relaxation oscillations and of the bursts (see Figure 8).

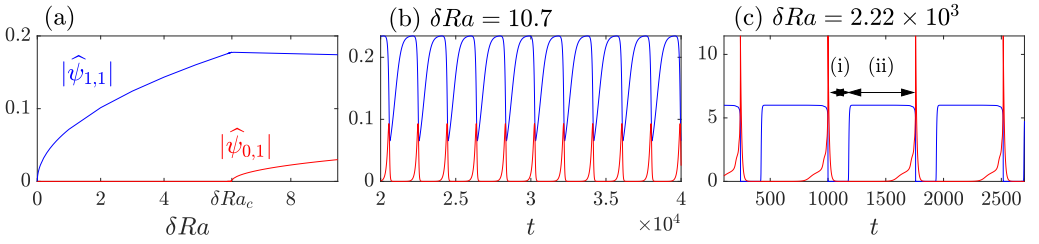

Figure 8: (a) Bifurcation diagram plotting $|\widehat{\psi}_{1,1}|$ (blue) and $|\widehat{\psi}_{0,1}|$ (red) against δRa with $Pr = 10^{-2}$. (b) and (c) display corresponding time series of $|\widehat{\psi}_{1,1}|$ and $|\widehat{\psi}_{0,1}|$ when $\delta Ra = 10.7$ and $\delta Ra = 2.2 \times 10^3$, respectively.

4. Weakly non-linear analysis at small Prandtl number

We perform a weakly non-linear analysis with the Prandtl number being our small parameter, $\epsilon = Pr \ll 1$. The analysis is carried out for arbitrary aspect ratio $\Gamma < 2^{4/3}\sqrt{1+2^{2/3}}$, and the other parameters and variables are scaled as follows:

$$Ra = Ra_c + r\epsilon^2 = \pi^4 \frac{(4+\Gamma^2)^3}{4\Gamma^4} + r\epsilon^2, \tag{4.1a}$$

$$t = \frac{\tau_O}{\epsilon} = \frac{\tau_E}{\epsilon^3}, \tag{4.1b}$$

$$\psi^E = \epsilon\psi_1^E(\tau_E, x, y) + \epsilon^2\psi_2^E(\tau_E, x, y) + \mathcal{O}(\epsilon^3), \tag{4.1c}$$

$$\theta^E = \epsilon\theta_1^E(\tau_E, x, y) + \epsilon^2\theta^E(\tau_E, x, y) + \mathcal{O}(\epsilon^3), \tag{4.1d}$$

$$\psi^O = \epsilon^2\psi_1^O(\tau_O, x, y) + \epsilon^3\psi_2^O(\tau_O, x, y) + \mathcal{O}(\epsilon^4), \tag{4.1e}$$

$$\theta^O = \epsilon^2\theta_1^O(\tau_O, x, y) + \epsilon^3\theta_2^O(\tau_O, x, y) + \mathcal{O}(\epsilon^4). \tag{4.1f}$$

We have introduced two time-scales τ_O and τ_E, due to the distinct time-scale separation between the odd and even modes, observed for example in Figure 8(c). Equation (4.1*a*) is inspired by the power law $\delta Ra \propto Pr^2$. The scalings of the dependent variables are constructed such that weak nonlinearity and coupling between even and odd modes enter at the same order, as we will see below.

First we examine the evolution of the even modes. At $\mathcal{O}(\epsilon)$ and $\mathcal{O}(\epsilon^2)$ we find

$$\psi_1^E = \frac{4+\Gamma^2}{\Gamma}\pi A \sin(2\pi x/\Gamma)\sin(\pi y), \tag{4.2a}$$

$$\theta_1^E = 2A\cos(2\pi x/\Gamma)\sin(\pi y), \tag{4.2b}$$

and

$$\psi_2^E = 0, \tag{4.3a}$$

$$\theta_2^E = -\pi A^2 \frac{4+\Gamma^2}{2\Gamma^2}\sin(2\pi y), \tag{4.3b}$$

which describe the asymptotic behaviour of the SCRS as $\delta Ra \to 0$.

At $\mathcal{O}(\epsilon^3)$, we have

$$\nabla^2\psi_{1\tau_E}^E + \{\psi_1^O, \nabla^2\psi_1^O\} = Ra_c\theta_{3x}^E + \nabla^4\psi_3^E + r\theta_{1x}^E, \tag{4.4a}$$

$$\{\psi_1^E, \theta_2^E\} = \psi_{3x}^E + \nabla^2\theta_3^E, \tag{4.4b}$$

the solvability condition for which gives us

$$\frac{(4+\Gamma^2)^2}{2\Gamma^3}\pi^3\,\frac{\mathrm{d}A}{\mathrm{d}\tau_E} - r\frac{2\pi}{\Gamma}A + \frac{(4+\Gamma^2)^4}{4\Gamma^7}\pi^7 A^3 = \frac{2\mathrm{i}}{\Gamma}\left\langle\{\psi_1^O, \nabla^2\psi_1^O\}, \phi_{1,1}\right\rangle. \tag{4.5}$$

The right-hand side of equation (4.5) is the inner product of the nonlinear forcing term with the $(1,1)$ basis function, and captures the net effect of the odd modes on the amplitude A of the dominant even mode. If this term is set to zero, then equation (4.5) reduces to the standard Landau equation governing the amplitude A of weakly nonlinear perturbations to the static conduction state (Fowler 1997).

To evaluate the right-hand side of equation (4.5), we now turn to the odd modes. At lowest order we obtain the problem

$$\nabla^2\psi^O_{1\tau_O} + \{\psi_1^O, \nabla^2\psi_1^E\} + \{\psi_1^E, \nabla^2\psi_1^O\} = Ra_c\theta^O_{1x} + \nabla^4\psi_1^O, \tag{4.6a}$$

$$0 = \psi^O_{1x} + \nabla^2\theta_1^O, \tag{4.6b}$$

which can be reduced to

$$\nabla^2\psi^O_{1\tau_O} + \frac{\pi(4+\Gamma^2)}{\Gamma}A\left\{\sin\left(\frac{2\pi x}{\Gamma}\right)\sin(\pi y), \nabla^2\psi_1^O + \frac{\pi^2(4+\Gamma^2)}{\Gamma^2}\psi_1^O\right\} = \nabla^4\psi_1^O - Ra_c\nabla^{-2}\psi^O_{1xx}. \tag{4.7}$$

Using the Fourier decomposition (2.4), i.e.

$$\psi_1^O = \sum_{k_x+k_y\in 2\mathbb{Z}+1}\widehat{\psi}_{k_x,k_y}\phi_{k_x,k_y}, \tag{4.8}$$

we can express equation (4.7) as a linear dynamical system of the form

$$\frac{\mathrm{d}\boldsymbol{\psi}_1^O}{\mathrm{d}\tau_O} = (AM + D)\boldsymbol{\psi}_1^O. \tag{4.9}$$

Here M and D are known constant matrices, calculated as described in Appendix C, and $\boldsymbol{\psi}_1^O = (\widehat{\psi}_{k_x,k_y})_{k_x+k_y\in 2\mathbb{Z}+1}$ is the vector of odd modes.

We recall that A evolves on the much slower time-scale $\tau_E = \epsilon^2\tau_O$. As justified in Appendix C, to leading order in ϵ, it follows that $\boldsymbol{\psi}_1^O$ is proportional to the most unstable eigenvector of the problem (4.9). We can therefore write

$$\boldsymbol{\psi}_1^O(\tau_O; A) \sim B(\tau_O)\boldsymbol{v}(A), \tag{4.10}$$

where

$$(AM + D)\boldsymbol{v}(A) = \sigma(A)\boldsymbol{v}(A), \tag{4.11}$$

with $\sigma(A)$ the eigenvalue of (4.11) with the largest real part, and $\boldsymbol{v}$ normalised such that $||\boldsymbol{v}|| = 1$. At leading order in ϵ, the net amplitude B of the odd modes thus evolves according to

$$\frac{\mathrm{d}B}{\mathrm{d}\tau_O} = \sigma(A)B. \tag{4.12}$$

With ψ_1^O decomposed as in (4.10), we can express the right-hand side of equation (4.5) in the form

$$\frac{2\mathrm{i}}{\Gamma}\left\langle\{\psi_1^O, \nabla^2\psi_1^O\}, \phi_{1,1}\right\rangle = -B^2\lambda(A), \tag{4.13}$$

where

$$\lambda(A) = -\frac{2\mathrm{i}}{\Gamma}\left\langle\{v(A), \nabla^2 v(A)\}, \phi_{1,1}\right\rangle. \tag{4.14}$$

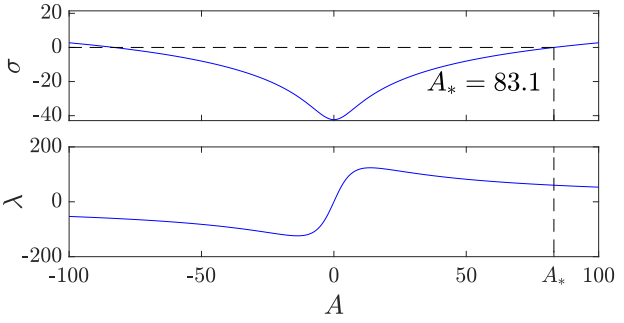

Figure 9: The functions $\sigma(A)$ and $\lambda(A)$ as they appear in (4.16) with $\Gamma = 2$. Highlighted is the point A_* at which $\sigma(A_*) = 0$.

For a given value of Γ, the functions $\sigma(A)$ and $\lambda(A)$ can both be computed once-and-for-all from equations (4.11) and (4.14). Equations (4.5) and (4.12) then provide a closed two-dimensional autonomous system for the amplitudes A and B of the even and odd modes, respectively.

By using the scalings

$$A = \left(\frac{4\Gamma^7}{(4+\Gamma^2)^4\pi^7}\right)^{1/3}\widehat{A} = a\widehat{A}, \qquad B = a\frac{(4+\Gamma^2)^2}{2\Gamma^3}\pi^3\widehat{B} = b\widehat{B},$$
$$r = \frac{\Gamma}{2\pi a}\widehat{r}, \qquad \tau_E = b\widehat{\tau_E}, \qquad \lambda = \frac{\widehat{\lambda}}{b^2}, \qquad \sigma = \frac{\widehat{\sigma}}{b}, \tag{4.15}$$

we normalise the system (4.5) and (4.12) and are left with the two ODEs (after dropping hats)

$$\dot{A} = rA - A^3 - B^2\lambda(A), \tag{4.16a}$$
$$\epsilon^2\dot{B} = \sigma(A)B, \tag{4.16b}$$

where the time derivative is taken with respect to the slow time-scale τ_E. In Figure 9 we show the functions $\sigma(A)$ and $\lambda(A)$ (normalised according to (4.15)) in the instance when $\Gamma = 2$. The highlighted point A_* where $\sigma(A_*) = 0$ takes the value $A_* \approx 83.1$.

Since $\sigma(A)$ is an even function and $\lambda(A)$ is an odd function, we need only consider solutions of the phase plane problem (4.16) in the quadrant $A, B \geqslant 0$. The critical points are:

(i) $(A, B) = (0, 0)$, corresponding to the pure conduction state, which loses stability through the primary pitchfork bifurcation as r increases through zero. This bifurcation excites the even modes in the system.

(ii) $(\sqrt{r}, 0)$ exists for $r > 0$ and represents the SCRS, with no odd modes. This state loses stability through a secondary pitchfork bifurcation at $r = r_c = A_*^2 \approx 6.91 \times 10^3$ (when $\Gamma = 2$), at which point the SCRS becomes unstable to odd perturbations.

(iii) $(A_*, \sqrt{(rA_* - A_*^3)/\lambda(A_*)})$ exists for $r > r_c$, when a mixed steady state including odd and even modes emerges. Finally, this steady state loses stability in a Hopf bifurcation at $r = r_* = A_*^2 + (2A_*^2\lambda(A_*))/(\lambda(A_*) - A_*\lambda'(A_*))$. When $\Gamma = 2$, we calculate $r_* \approx 1.53 \times 10^4$.

We can use the value of r_c from (ii) to infer the prefactor in the power law found in §4 for the stability boundary at small Pr. Rescaling back to our original variables using (4.15), we find that $r_c = \delta Ra_c/Pr^2 \approx 6.35 \times 10^4$ which indeed gives excellent agreement with the fit obtained in Figure 7.

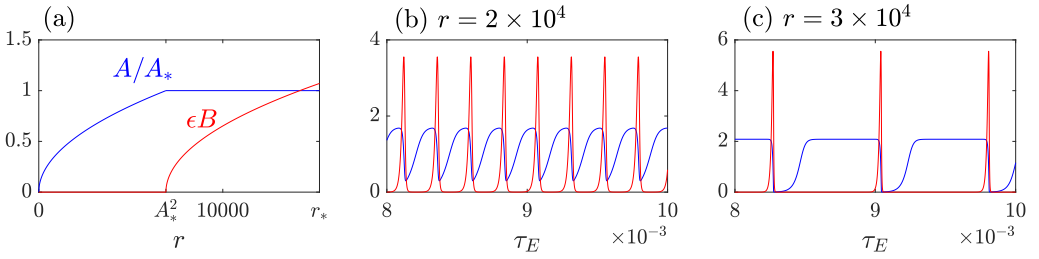

Figure 10: (a) Bifurcation diagram plotting A/A_* (blue) and ϵB (red) against r with $\Gamma = 2$ and $\epsilon = 10^{-2}$. Annotated are $r = r_c = A_*^2$, the point of the secondary pitchfork bifurcation and $r = r_*$, where the Hopf bifurcation occurs. (b) and (c) display time series of A/A_* and ϵB when $r = 2 \times 10^4$ and $r = 3 \times 10^4$, respectively.

To see the bifurcations itemized above in practice, we solve equations (4.16) numerically. Figure 10(a) is a bifurcation diagram showing how the nontrivial steady states identified in (ii) and (iii) above emerge at $r = 0$ and $r = r_c = A_*^2$, respectively. The Hopf bifurcation occurs at $r = r_*$, beyond which point the system undergoes the nonlinear relaxation oscillations and bursts displayed in Figures 10(b) and (c) for $r = 2 \times 10^4$ and $r = 3 \times 10^4$, respectively.

There is great qualitative agreement between the behaviours of our vastly simplified two-dimensional system and of the full system, displayed in Figures 10 and 8, respectively. Although the system (4.16) was formally derived in the asymptotic limit as $Pr \to 0$, similar relaxation oscillations are found in many parts of the (Pr, Ra)-plane (Goluskin *et al.* 2014). The resemblance of these oscillations to the behaviour of simple predator-prey population models and the Lotka–Volterra equations has often been studied (Leboeuf *et al.* 1993; Garcia *et al.* 2003; Decristoforo *et al.* 2020; Malkov *et al.* 2001). In this analogy, the place of the predator population is taken by a quantity undergoing relaxation oscillations, and the place of the prey population is taken by a bursting quantity. In contrast, our model (4.16) has been derived systematically from the governing equations without the need for any *ad hoc* closure assumptions.

5. Stability at large Prandtl number

Figure 11 displays the (Pr, Ra)-plane for $10^5 < Pr < 10^6$, highlighting where the SCRS is stable (white, S) or unstable (blue, US). At $q_4 = (7 \times 10^5, 2.54 \times 10^7)$ there is a corner in the stability boundary and two complex conjugate pairs of eigenvalues cross the imaginary axis simultaneously as was discussed in §3.

The stability boundaries for the two most unstable eigenfunctions therefore cross at q_4, as indicated by the dashed curves in the inset in Figure 11. As noted in §3, the *symmetry breaking* eigenfunction (labelled E_{SB}) that is excited as we cross the red dashed curve has the property that $\widehat{\psi}^o_{k_x,k_y}$ and $\mathrm{i}\widehat{\theta}^o_{k_x,k_y}$ are purely real and therefore breaks the reflection symmetry between counter-rotating convection rolls in the SCRS. It follows that the horizontal velocity is an even function of x which allows for instantaneous zonal flow in the solution.

The *period doubling* eigenfunction (labelled E_{PD}) corresponding to the green dashed curve has the complementary symmetry that $\widehat{\psi}^o_{k_x,k_y}$ and $\mathrm{i}\widehat{\theta}^o_{k_x,k_y}$ are pure imaginary, and the zonal modes are therefore all zero: $\widehat{\psi}^o_{0,k_y} = 0$ for all k_y. The horizontal velocity is now an odd function of x and, although the E_{PD} eigenfunction introduces odd modes to the solution, it does not break the reflection symmetry (2.10) in the SCRS, but instead causes

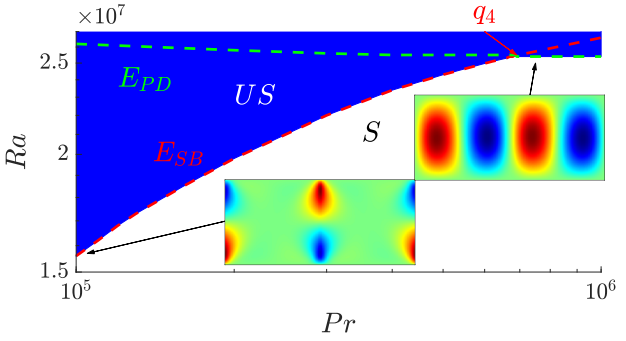

Figure 11: The (Pr, Ra) parameter space for large Pr highlighting when the SCRS is linearly stable (white, S) and unstable (blue, US). The point q_4 is where the stability boundaries corresponding to the symmetry breaking (red, E_{SB}) and period doubling (green, E_{PD}) eigenfunctions cross. The inserts show the odd eigenfunctions, ψ^O, associated with E_{SB} and E_{PD} where red, green and blue indicate $\psi^O > 0$, $\psi^O \approx 0$ and $\psi^O < 0$, respectively. The parameters are $(Ra, Pr) = (1.56 \times 10^7, 10^5)$ and $(Ra, Pr) = (2.54 \times 10^7, 7 \times 10^5)$.

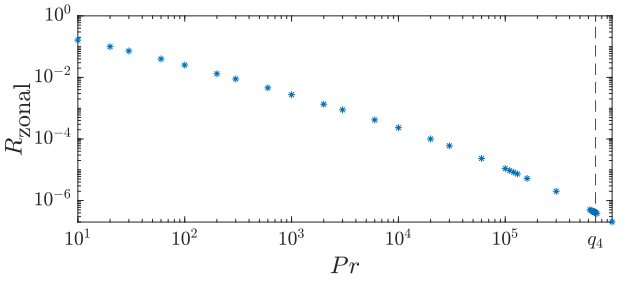

Figure 12: The proportion of energy held in zonal modes, R_{zonal} defined in (5.1), in the eigenfunction E_{SB} at the stability threshold plotted versus Pr. The red dashed line highlights the point q_4 beyond which the eigenfunction E_{PD}, with no zonal modes, becomes the most unstable.

a period doubling in x. Consequently, zonal modes at the instability switch off as we pass the point q_4. The qualitative change in the structure of the dominant eigenfunction is demonstrated by the inserts in Figure 11, and movies showing how these eigenfunctions evolve in time are included in the Supplementary Material (https://doi.org/10.1017/...).

To measure the proportion of energy held in zonal modes in the eigenfunction E_{SB}, we define

$$R_{\text{zonal}} = \frac{\sum_{k_x} \left| K_{k_x,0} \widehat{\psi}_{k_x,0} \right|^2}{\sum_{k_x,k_y} \left| K_{k_x,k_y} \widehat{\psi}_{k_x,k_y} \right|^2}, \tag{5.1}$$

where $K_{k_x,k_y} = \sqrt{(2\pi k_x/\Gamma)^2 + (\pi k_y)^2}$ is the non-dimensional wavenumber. As shown in Figure 12, R_{zonal} decreases as we increase Pr along the stability boundary. Nevertheless, E_{SB} still has a small but nonzero zonal component at the point q_4 where the eigenfunction

E_{PD} takes over and zonal modes disappear completely. The instance of E_{SB} in figure 11 is at the large Prandtl number $Pr = 10^5$, and hence the zonal modes do not carry much energy. In the Supplementary Material (https://doi.org/10.1017/...), there is a video of E_{SB} with $Pr = 100$ (Movie 6), in which case the presence of zonal modes is clear.

As we increase the Prandtl number past q_4, the green dashed line in Figure 11 appears to approach a limiting value $Ra = 2.54 \times 10^7$, at which the SCRS is unstable for all Pr. To examine this statement, we consider the $Pr \to \infty$ limit in which the governing equations (2.1) reduce to

$$\nabla^4 \psi = -Ra\theta_x, \tag{5.2a}$$

$$\theta_t + \{\psi, \theta\} = \psi_x + \nabla^2 \theta. \tag{5.2b}$$

We analyse the linear stability of the SCRS for the reduced system (5.2) as in §3, and we find that it becomes unstable at $Ra = 2.54 \times 10^7$, consistently with the results presented in Figure 11. It is clear from (5.2a) that $\widehat{\psi}_{0,k_y} = 0$ in the $Pr \to \infty$ limit, again in agreement with the period doubling eigenfunction identified above. We conclude that $Pr > 7 \times 10^5$ is a large enough Prandtl number such that the system exhibits the asymptotic behaviour of identically zero zonal modes, at least linearly at the SCRS instability.

We note that the disparity between the thermal and viscous time-scales makes it very difficult to reproduce the behaviour close to q_4 using DNS. The linear stability analysis predicts that E_{PD} oscillates with a frequency of order 10 with respect to the thermal time-scale, and it is therefore necessary to integrate the underlying equations over at least $Pr/10 \approx 7 \times 10^4$ viscous time units to observe just one complete oscillation. At the required spatial resolution, it proved unfeasible to compute enough cycles to reliably observe the exponential growth or decay associated with the Hopf bifurcation.

6. Conclusions

This article concerns 2D Rayleigh–Bénard convection with free-slip boundaries and horizontal periodicity. The horizontal periodicity permits so-called zonal flow, with horizontal wavenumber equal to zero. When present, the zonal flow can dominate the flow, significantly suppress convective heat transfer (Goluskin *et al.* 2014) and undergo random-in-time reversals (Winchester *et al.* 2021). The onset of zonal flow is therefore of great importance.

With aspect ratio $\Gamma = 2$ and increasing Rayleigh number, the first state to be excited as the pure conducting state loses stability consists of steady convection rolls, referred to in the text as the SCRS. The SCRS consists of only so-called even modes and becomes unstable to odd modes as the Rayleigh number is increased. We determine the stability boundary in the (Pr, Ra)-plane and identify corners and cusps in the boundary where qualitative changes occur to the most unstable eigenfunction. We observe three regions where the SCRS loses and subsequently regains stability as the Rayleigh number is increased. Such behaviour seems to defy our intuition that increasing the importance of buoyancy relative to viscous and thermal dissipation should make the system less stable, although we note that reorganisation with increasing Ra has been observed experimentally by Fauve *et al.* (1984) in convective flow of mercury at small Prandtl number.

The excitation of odd modes is necessary, but not sufficient, for net zonal flow to exist. The possible qualitative behaviours in our system are delineated by the points q_1 and q_4 identified in the parameter space shown in Figure 2. Below and to the left of point q_1, the SCRS loses stability through a pitchfork bifurcation, and the resulting steady

shear flow then itself becomes unstable and undergoes nonlinear oscillations and bursts. In either case the system produces a net zonal flow. On the other hand, to the right of point q_4, the dominant unstable odd eigenfunction preserves the reflection symmetry in the SCRS, and the zonal flow is identically zero.

Between points q_1 and q_4, the initial instability occurs through a Hopf bifurcation leading to oscillations in which the direction of the shear flow alternates (Rucklidge & Matthews 1996). In this case, although the solution exhibits zonal flow instantaneously, the net (time-averaged) zonal flow is zero. This range includes the case $Pr = 30$ for which Winchester *et al.* (2021) showed that the initial Hopf bifurcation is the first stage of a process that ultimately results in either persistent or intermittent zonal flow in the turbulent regime. We find that zonal modes become less prominent in the most unstable odd eigenfunction as the Prandtl number increases, but are still present up to $Pr = 7 \times 10^5$, when they abruptly switch off at point q_4.

As $Pr \to 0$, the SCRS becomes unstable almost immediately as a new steady state, consisting of both even and odd modes, emerges in a pitchfork bifurcation. We observe a power-law $\delta Ra \propto Pr^2$ along the stability boundary. With a weakly non-linear analysis, we derive a two-dimensional approximate model that successfully predicts the power-law in the stability boundary, including its prefactor, as well as the non-linear relaxation oscillations and bursts observed in DNS at low Pr.

At large Prandtl numbers, we observe a corner in the stability boundary at $q_4 = (7 \times 10^5, 2.54 \times 10^7)$ where the zonal modes in the most unstable eigenfunction switch off. As the Prandtl number increases beyond q_4, the stability boundary converges to the asymptotic value $Ra = 2.54 \times 10^7$. This observation is consistent with formally taking the $Pr \to \infty$ limit, which completely removes zonal modes. Our conclusion is that no zonal modes are excited at the SCRS instability boundary for Prandtl numbers greater than 7×10^5. Instead, an unsteady state is produced consisting of both even and odd modes. It remains open to determine when this state in turn becomes susceptible to growing zonal perturbations.

We focus here on the case of aspect ratio $\Gamma = 2$. Further analysis of the weakly nonlinear model (4.16) suggests that the type and sequence of bifurcations that occur in the small-Pr limit may be completely different for different values of Γ. At large Pr, both the asymptotic value of the Rayleigh number and the Prandtl number at which zonal modes switch off at onset can depend on the geometry and the boundary conditions. For general Prandtl number, we can anticipate that the structure of the stability boundary and the properties of the excited solutions also depend significantly on the value of Γ. In particular, if $\Gamma \geqslant 2^{4/3}\sqrt{1 + 2^{2/3}}$ then both odd and even modes become excited as Ra increases past Ra_c, and it is no longer clear that the odd/even mode decomposition which proves so convenient in our set-up is still able to give some insight.

Supplementary data. Supplementary material and movies are available at https://doi.org/10.1017/...

Acknowledgements. We are grateful for the feedback from three anonymous referees, whose helpful suggestions significantly improved this paper. P.W. gratefully acknowledges funding from the Engineering and Physical Sciences Research Council and from the Society of Swedish Engineers in Great Britain.

Declaration of interests. The authors report no conflict of interest.

Appendix A. Computation of the SCRS

We wish to find a solution $(\psi^E,\, \theta^E)$ of the steady "even" problem (2.9). We expand both ψ^E and θ^E as in (2.4), i.e. in modes of the form

$$\phi_{k_x,k_y}(x,y) = \mathrm{e}^{2\pi \mathrm{i} k_x x/\Gamma}\sin(\pi k_y y), \qquad k_x + k_y \in 2\mathbb{Z}, \tag{A 1}$$

and define the inner product

$$\langle \phi_{k_{x_1},k_{y_1}}, \phi_{k_{x_2},k_{y_2}} \rangle = \int_0^1 \int_0^\Gamma \phi_{k_{x_1},k_{y_1}} \phi^*_{k_{x_2},k_{y_2}} \,\mathrm{d}x\,\mathrm{d}y = \frac{\Gamma}{2}\delta_{k_{x_1},k_{x_2}}\delta_{k_{y_1},k_{y_2}}. \tag{A 2}$$

Acting with this inner product on equations (2.9) we find, for each (k_x, k_y),

$$\frac{\mathrm{i}}{2}\sum_{\substack{k_{x_1}+k_{x_1}=k_x\\ |k_{y_1}\pm k_{y_2}|=k_y}} \widehat{\psi}_{k_{x_1},k_{y_1}}\widehat{\psi}_{k_{x_2},k_{y_2}} K^2_{k_{x_2},k_{y_2}} G(k_{x_1},k_{x_2},k_{y_1},k_{y_2}) + \mathrm{i}k_x Ra Pr \widehat{\theta}_{k_x,k_y} + Pr K^4_{k_x,k_y}\widehat{\psi}_{k_x,k_y} = 0, \tag{A 3a}$$

$$\frac{\mathrm{i}}{2}\sum_{\substack{k_{x_1}+k_{x_1}=k_x\\ |k_{y_1}\pm k_{y_2}|=k_y}} \widehat{\psi}_{k_{x_1},k_{y_1}}\widehat{\theta}_{k_{x_2},k_{y_2}} G(k_{x_1},k_{x_2},k_{y_1},k_{y_2}) - \mathrm{i}k_x\widehat{\psi}_{k_x,k_y} + K^2_{k_x,k_y}\widehat{\theta}_{k_x,k_y} = 0, \tag{A 3b}$$

where we have introduced the wavenumber and the functions

$$K_{k_x,k_y} = \sqrt{\Big(\frac{2\pi}{\Gamma}k_x\Big)^2 + (\pi k_y)^2}, \tag{A 4a}$$

$$G(k_{x_1},k_{y_1},k_{x_2},k_{y_2},k_y) = \frac{2\pi^2}{\Gamma}\big(k_{x_1}k_{y_2}h(k_{y_2},k_{y_1},k_y) - k_{y_1}k_{x_2}h(k_{y_1},k_{y_2},k_y)\big), \tag{A 4b}$$

$$h(x,y,z) = \begin{cases} -1 & \text{if } x = y+z,\\ 1 & \text{otherwise.}\end{cases} \tag{A 4c}$$

The quadratic system of algebraic equations (A 3) is solved using Newton's method repeated as

$$v_{n+1} = v_n - J^{-1}(v_n)f(v_n), \tag{A 5}$$

where v_n is a vector of the ψ and θ modes, $f(v_n)$ and $J(v_n)$ are the LHS of (A 3) and its Jacobian evaluated at v_n, respectively, and v_{n+1} is a vector containing the subsequent values of the modes following one iteration. We utilise the reflection symmetry (2.10) of the SCRS to reduce the number of unknowns.

For all computations in this study, we use an equal number N of Fourier modes in both x and y. So that our results are consistent with those from the DNS, we employ the two-thirds dealiasing rule, meaning that the largest retained wavenumbers in x and y are $N/3$ and $2N/3$, respectively. The values of N used for different values of Ra are listed in Table 1.

To validate our computations of the SCRS, in the Supplementary Materials (https://doi.org/10.1017/...) we list the Nusselt number obtained for parameter values in the range $(Pr, Ra) \in [10^{-6}, 10^6] \times (8\pi^4, 10^8]$, demonstrating excellent agreement with results presented previously (Wen *et al.* 2020).

N	Ra
64	$(8\pi^4, 3\times10^3]$
152	$(3\times10^3, 6\times10^5]$
256	$(6\times10^5, 4\times10^6]$
400	$(4\times10^6, 10^8]$

Table 1: Resolution (N) used in all computations in the DNS, Newton's method to find the SCRS, and the linear stability analysis, for $Ra \in (8\pi^4, 10^8]$.

Appendix B. Linear stability analysis

Here, we provide further details of the linear stability analysis discussed in §3. For given Ra and Pr, we construct a steady solution (ψ^E, θ^E) to the even system (2.9) as described in Appendix A. Odd perturbations to this steady state satisfy the "odd" part of the Boussinesq equations, namely the linear, time-autonomous system of PDEs (2.7). We make the ansatz (3.1) and act on (2.7) with the inner product (A 2) to obtain an eigenvalue problem for the odd growth rate σ^o, namely

$$\frac{\mathrm{i}}{2}\sum_{\substack{k_{x_o}+k_{x_E}=k_x\\ |k_{y_o}\pm k_{y_E}|=k_y}} \widehat{\psi}^o_{k_{x_o},k_{y_o}}\widehat{\psi}^E_{k_{x_E},k_{y_E}}G(k_{x_E},k_{y_E},k_{x_o},k_{y_o},k_y)\left[K^2_{k_{x_o},k_{y_o}}-K^2_{k_{x_E},k_{y_E}}\right]$$
$$-\mathrm{i}k_x RaPr\widehat{\theta}^o_{k_x,k_y}-PrK^4_{k_x,k_y}\widehat{\psi}^o_{k_x,k_y}=\sigma^o K^2_{k_x,k_y}\widehat{\psi}^o_{k_x,k_y}, \quad (\mathrm{B}\,1a)$$

$$\frac{\mathrm{i}}{2}\sum_{\substack{k_{x_o}+k_{x_E}=k_x\\ |k_{y_o}\pm k_{y_E}|=k_y}} \left[\widehat{\theta}^o_{k_{x_o},k_{y_o}}\widehat{\psi}^E_{k_{x_E},k_{y_E}}-\widehat{\psi}^o_{k_{x_o},k_{y_o}}\widehat{\theta}^E_{k_{x_E},k_{y_E}}\right]G(k_{x_E},k_{y_E},k_{x_o},k_{y_o},k_y)$$
$$+\mathrm{i}k_x\widehat{\psi}^o_{k_x,k_y}-K^2_{k_x,k_y}\widehat{\theta}^o_{k_x,k_y}=\sigma^o\widehat{\theta}^o_{k_x,k_y}. \quad (\mathrm{B}\,1b)$$

where K^2, G and h are as in (A 4).

Similarly, for even perturbations, we let $\psi=\psi^E+\delta\psi^e e^{\sigma^e t}$ and $\theta=\theta^E+\delta\theta^e e^{\sigma^e t}$, and linearise (2.8) with respect to δ to obtain the same system as in (B 1), but with $o\mapsto e$.

Appendix C. Weakly non-linear analysis

In this appendix, we provide some details on the construction of the eigenvalue problem (4.9) and the derivation of the amplitude equation (4.12) for the odd modes.

First, substitution of the decomposition (4.8) into the first-order odd equation (4.7) results in the linear system

$$\frac{\mathrm{d}\widehat{\psi}_{k_x,k_y}}{\mathrm{d}\tau_O}=A(\tau_E)\sum_{(n,m)\in S}\frac{\pi\Gamma}{2}\left(K^2_{n,m}-\frac{K^4_{1,1}}{K^2_{n,m}}\right)\big(nh(n,k_x,1)-mh(m,k_y,1)\big)\widehat{\psi}_{n,m}$$
$$+\frac{\Gamma}{2}\left(\frac{4\pi^2Ra_c k_x^2}{\Gamma^2K^4_{k_x,k_y}}-K^2_{k_x,k_y}\right)\widehat{\psi}_{k_x,k_y}, \quad (\mathrm{C}\,1)$$

where S denotes the set

$$S=\big\{(k_x+1,k_y+1),(k_x-1,k_y+1),(k_x+1,k_y-1),(k_x-1,k_y-1)\big\}, \quad (\mathrm{C}\,2)$$

and $K^2_{k_x,k_y}$ and h are as in (A 4). The first and second terms on the right-hand side of equation (C 1) respectively define the elements of the matrix M and of the diagonal matrix D in equation (4.9), which takes the form

$$\epsilon^2 \frac{\mathrm{d}\boldsymbol{\psi}_1^O}{\mathrm{d}\tau_E} = \big(A(\tau_E)M + D\big)\boldsymbol{\psi}_1^O \tag{C 3}$$

on the slow time-scale τ_E.

We seek the solution for $\boldsymbol{\psi}_1^O$ as a WKB asymptotic expansion of the form

$$\boldsymbol{\psi}_1^O(\tau_E) \sim \mathrm{e}^{\varphi(\tau_E)/\epsilon^2}\boldsymbol{C}(\tau_E;\epsilon) \sim \mathrm{e}^{\varphi(\tau_E)/\epsilon^2}\sum_n \boldsymbol{C}_n(\tau_E)\epsilon^{2n}, \tag{C 4}$$

following which (C 3) becomes

$$(\dot{\varphi} I - A(\tau_E)M - D)\,\boldsymbol{C} + \epsilon^2\dot{\boldsymbol{C}} = \boldsymbol{0}. \tag{C 5}$$

To leading order in ϵ, we find that $\dot{\varphi} = \sigma(A)$ and $\boldsymbol{C}_0 = b(\tau_E)\boldsymbol{v}(A)$, where σ and $\boldsymbol{v}$ satisfy the eigenvalue problem

$$(\sigma I - AM - D)\,\boldsymbol{v} = \boldsymbol{0}. \tag{C 6}$$

For a modal truncation such that our system is of size N we (in general) have N eigenvalues $\sigma_j(A)$, ordered such that $\mathcal{R}(\sigma_j(A)) \geqslant \mathcal{R}(\sigma_{j+1}(A))$, and corresponding eigenvectors $\boldsymbol{v}_j(A)$, assumed to be normalised such that $\|\boldsymbol{v}_j(A)\|_{l^2} = 1$. The general leading order solution for $\boldsymbol{\psi}_1^O$ is then

$$\boldsymbol{\psi}_1^O(\tau_E) \sim \sum_{j=1}^{N} b_j(\tau_E)\mathrm{e}^{\varphi_j(\tau_E)/\epsilon^2}\boldsymbol{v}_j\big(A(\tau_E)\big), \tag{C 7}$$

with $\dot{\varphi}_j(\tau_E) = \sigma_j(A(\tau_E))$.

Since $\mathcal{R}(\sigma_j) \geqslant \mathcal{R}(\sigma_{j+1})$, the solution (C 7) is dominated by the first term in the sum. In fact, we observe that the dominant eigenvalue σ_1 is real and that $\mathcal{R}(\sigma_2) < 0$, meaning that all terms except the first are exponentially small after a short transient. We thus have

$$\boldsymbol{\psi}_1^O(\tau_E) \sim B(\tau_E)\boldsymbol{v}_1\big(A(\tau_E)\big), \tag{C 8}$$

where the leading-order amplitude is given by $B(\tau_E) = b_1(\tau_E)e^{\varphi_1(\tau_E)/\epsilon^2}$. Taking derivatives with respect to τ_E leaves us with

$$\epsilon^2\dot{B}(\tau_E) \sim \sigma_1\big(A(\tau_E)\big)B + O(\epsilon^2), \tag{C 9}$$

which is equivalent to equation (4.12). An equation for b_1 can be obtained in principle from the solvability condition for $\boldsymbol{C}_1$ in (C 5), but does not affect the leading-order evolution of B.

REFERENCES

Aoyagi, T., Yagi, M. & Itoh, S.-I 1997 Comparison analysis of lorenz model and five components model. *Journal of the Physical Society of Japan* **66** (9), 2689–2701.

Berning, M. & Spatschek, K. H. 2000 Bifurcations and transport barriers in the resistive-g paradigm. *Phys. Rev. E* **62**, 1162–1174.

Bolton, E. W. & Busse, F. H. 1985 Stability of convection rolls in a layer with stress-free boundaries. *J. Fluid Mech.* **150**, 487–498.

Busse, F.H. 1983 Generation of mean flows by thermal convection. *Physica D: Nonlinear Phenomena* **9** (3), 287–299.

Busse, F. H. 1967 On the stability of two-dimensional convection in a layer heated from below. *Journal of Mathematics and Physics* **46** (1-4), 140–150.

Busse, F. H. & Bolton, E. W. 1984 Instabilities of convection rolls with stress-free boundaries near threshold. *J. Fluid Mech.* **146**, 115–125.

Chandra, M. & Verma, M. K. 2011 Dynamics and symmetries of flow reversals in turbulent convection. *Phys. Rev. E* **83**, 067303.

Decristoforo, G., Theodorsen, A. & Garcia, O. E. 2020 Intermittent fluctuations due to lorentzian pulses in turbulent thermal convection. *Phys. Fluids* **32** (8), 085102.

Diamond, P H, Itoh, S-I, Itoh, K & Hahm, T S 2005 Zonal flows in plasma—a review. *Plasma Physics and Controlled Fusion* **47** (5), R35–R161.

Fauve, S., Laroche, C., Libchaber, A. & Perrin, B. 1984 Chaotic phases and magnetic order in a convective fluid. *Phys. Rev. Lett.* **52**, 1774–1777.

Fowler, A. C. 1997 *Mathematical Models in the Applied Sciences*. Cambridge University Press.

Fuentes, J. R. & Cumming, A. 2021 Shear flows and their suppression at large aspect ratio: Two-dimensional simulations of a growing convection zone. *Phys. Rev. Fluids* **6**, 074502.

Fujisawa, A. 2008 A review of zonal flow experiments. *Nuclear Fusion* **49**, 013001.

Garcia, O. E., Bian, N. H., Paulsen, J.-V., Benkadda, S. & Rypdal, K. 2003 Confinement and bursty transport in a flux-driven convection model with sheared flows. *Plasma Physics and Controlled Fusion* **45** (6), 919–932.

Goluskin, D., Johnston, H., Flierl, G. R. & Spiegel, E. A. 2014 Convectively driven shear and decreased heat flux. *J. Fluid Mech.* **759**, 360.

Heimpel, M., Aurnou, J. & Wicht, J. 2005 Simulation of equatorial and high-latitude jets on jupiter in a deep convection model. *Nature* **438**, 193–6.

Hermiz, K. B., Guzdar, P. N. & Finn, J. M. 1995 Improved low-order model for shear flow driven by rayleigh-bénard convection. *Phys. Rev. E* **51**, 325–331.

Horton, W., Hu, G. & Laval, G. 1996 Turbulent transport in mixed states of convective cells and sheared flows. *Physics of Plasmas* **3** (8), 2912–2923.

Howard, L. N. & Krishnamurti, R. 1986 Large-scale flow in turbulent convection: a mathematical model. *J. Fluid Mech.* **170**, 385–410.

Kaspi, Y., Galanti, E., Hubbard, W. B. & others 2018 Jupiter's atmospheric jet streams extend thousands of kilometres deep. *Nature* **555**, 223.

Kong, D., Zhang, K. & Schubert, G. 2018 Origin of jupiter's cloud-level zonal winds remains a puzzle even after juno. *Proc. Natl. Acad. Sci.* **115**, 201805927.

Krishnamurti, R. & Howard, L. N. 1981 Large-scale flow generation in turbulent convection. *Proc. Natl. Acad. Sci. U.S.A.* **78**, 1981.

Landsberg, A. S. & Knobloch, E. 1991 Direction-reversing traveling waves. *Physics Letters A* **159** (1), 17–20.

Leboeuf, J.-N., Charlton, L. A. & Carreras, B. A. 1993 Shear flow effects on the nonlinear evolution of thermal instabilities. *Phys. Fluids B* **5** (8), 2959–2966.

Malkov, M. A., Diamond, P. H. & Rosenbluth, M. N. 2001 On the nature of bursting in transport and turbulence in drift wave–zonal flow systems. *Phys. of Plasmas* **8** (12), 5073–5076.

Maximenko, N. A., Bang, B. & Sasaki, H. 2005 Observational evidence of alternating zonal jets in the world ocean. *Geophys. Res. Lett.* **32** (12), L12607.

Nadiga, B. T. 2006 On zonal jets in oceans. *Geophys. Res. Lett.* **33** (10).

Pal, P., Wahi, P., Paul, S., Verma, M. K., Kumar, K. & Mishra, P. K. 2009 Bifurcation and chaos in zero-prandtl-number convection. *EPL (Europhysics Letters)* **87** (5), 54003.

Paul, S., Verma, M. K., Wahi, P., Reddy, S. K. & Kumar, K. 2012 Bifurcation analysis of the flow patterns in two-dimensional Rayleigh-Bénard convection. *International Journal of Bifurcation and Chaos* **22** (05), 1230018.

Proctor, M. R. E. & Weiss, N. O. 1993 Symmetries of time-dependent magnetoconvection. *Geophysical & Astrophysical Fluid Dynamics* **70** (1-4), 137–160.

Rayleigh, Lord 1916 On convection currents in a horizontal layer of fluid, when the higher temperature is on the under side. *Phil. Mag* **32**, 529–546.

Read, P. L., Jacoby, T. N. L., Rogberg, P. H. T. & others 2015 An experimental study of multiple zonal jet formation in rotating, thermally driven convective flows on a topographic beta-plane. *Physics of Fluids* **27** (8), 085111.

Richards, K., Maximenko, N., Bryan, F. & Sasaki, H. 2006 Zonal jets in the pacific ocean. *Geophys. Res. Lett.* **33**.

Rucklidge, A. M. & Matthews, P. C. 1996 Analysis of the shearing instability in nonlinear convection and magnetoconvection. *Nonlinearity* **9**, 311–351.

Thompson, R. 1970 Venus's general circulation is a merry-go-round. *J. Atmos. Sci.* **27**, 1107.

Thual, O. 1992 Zero-prandtl-number convection. *Journal of Fluid Mechanics* **240**, 229–258.

Verma, M. K., Ambhire, S. C. & Pandey, A. 2015 Flow reversals in turbulent convection with free-slip walls. *Phys. Fluids* **27**, 047102.

Wang, Q., Chong, K. L., Stevens, R. J. A. M. & Lohse, D. 2020 From zonal flow to convection rolls in Rayleigh–Bénard convection with free-slip plates. *J. Fluid Mech.* **905**, A21.

Wen, B., Goluskin, D., LeDuc, M., Chini, G. P. & Doering, C. R. 2020 Steady rayleigh–bénard convection between stress-free boundaries. *Journal of Fluid Mechanics* **905**, R4.

Winchester, P., Dallas, V. & Howell, P. D. 2021 Zonal flow reversals in two-dimensional Rayleigh-Bénard convection. *Phys. Rev. Fluids* **6**, 033502.

Zhang, X., van Gils, D. P. M. & others 2020 Boundary zonal flow in rotating turbulent rayleigh-bénard convection. *Phys. Rev. Lett.* **124**, 084505.